Journal of Engineering and Technology for Industrial Applications

ITEGAM-JETIA

Manaus, v.12 n.58, p.884-894. March/April, 2026.
DOI: https://doi.org/10.5935/jetia.v12i58.3158

ISSN ONLINE: 2447-0228

RESEARCH ARTICLE OPEN ACCESS

A COMMUNICATION-FREE PQ-BASED CONTROL STRATEGY FOR 7.7 KW BIDIRECTIONAL WIRELESS EV CHARGERS

Abdelmoumin Hamrani[1], Abdelhalim Tlemçani[2] and Said Barkat[3]

[1]Laboratory of Advanced Electronic Systems (LSEA), University of Medea, Medea, Algeria.
[2]Electrical Engineering and Automation Research Laboratory (LREA), University of Medea, Medea, Algeria.
[3]Electrical Engineering Laboratory, Faculty of Technology, University of M'sila, M'sila, Algeria.

[1]https://orcid.org/0000-0003-4631-3160, [2]https://orcid.org/0000-0002-4385-671X, [3]https://orcid.org/0000-0002-6220-7387

Email: hamrani.abdelmoumin@univ-medea.dz, tlemcani.abdelhalim@univ-medea.dz, said.barkat@univ-msila.dz

ARTICLE INFO

Article History
Received: December 17, 2025
Reviewed: January 19, 2026
Accepted: March 10, 2026
Published: April 30, 2026

Keywords:
Bidirectional wireless power transfer (BD-WPT),
PQ-based control,
electric vehicle (EV) charging,
vehicle-to-grid (V2G),
grid-to-vehicle (G2V).

ABSTRACT

The widespread deployment of electric vehicles (EVs) has significantly heightened the need for more efficient and intelligent charging technologies. Bidirectional wireless power transfer (BD-WPT) systems enable both grid-to-vehicle (G2V) and vehicle-to-grid (V2G) operation, supporting applications such as renewable energy integration, demand peak mitigation, and system frequency stabilization. However, existing control strategies face challenges related to synchronization, communication delays, and robustness under detuning and misalignment. This paper investigates a PQ-based synchronization control technique for a 7.7 kW series–series compensated BD-WPT charger, designed in compliance with SAE J2954 standards. The adopted method relies solely on local measurements of active (P) and reactive (Q) power, eliminating the need for communication links while achieving decoupled control of power direction and magnitude. A voltage-controlled oscillator (VCO) ensures robust phase synchronization between the inverter and rectifier. Simulation results demonstrate that the PQ-based control achieves accurate bidirectional power transfer, seamless G2V/V2G transitions, effective power regulation, and resilience against detuning and coil misalignment. These findings underscore the promise of PQ-based synchronization in improving the efficiency, reliability, and scalability of BD-WPT systems for future smart grid integration.

I. INTRODUCTION

The growing penetration of EVs has intensified research efforts toward developing efficient and user-friendly charging infrastructures. Within this context, wireless power transfer (WPT) systems have been recognized as a viable and forward-looking approach, offering advantages in terms of convenience, safety, and compatibility with autonomous operation. While conventional unidirectional WPT systems are restricted to G2V energy transfer, BD-WPT systems provide the added capability of V2G operation, where energy stored in EV batteries can be returned to the grid. This bidirectional functionality is crucial for supporting peak load management, renewable energy integration, frequency regulation, and backup power supply, making BD-WPT a cornerstone technology for future smart grids [1], [2].

Recent advances in BD-WPT have significantly progressed the control of power flow direction and magnitude across various system architectures. A comprehensive review of constant current-constant voltage (CC-CV) charging strategies for resonant inductive power transfer (RIPT) systems classifies control methods into primary, secondary, and dual side approaches. However, these methods face challenges in accurately estimating load resistance and mutual inductance, as well as communication delays and losses, which can reduce control robustness and system efficiency [3]. To address misalignment issues, innovative compensation techniques based on inherent resonance frequency tracking have improved stability in bidirectional electrical coupling WPT (EC-WPT) systems.

Yet, these methods still require further validation for scalability and broader application scenarios, indicating current limitations in practical deployment [4]. In [5] the perturbation and observation technique was applied for dualside phase-shift control; however, discrepancies between the control clocks may cause the primary and secondary sides to operate at different switching frequencies. The study [6] introduces a communication-assisted strategy for managing BD-WPT systems, enabling inverter–rectifier synchronization without current sensing. However, this approach enables low-latency and efficient bidirectional power flow regulation via a specialized wireless communication link between the primary and secondary sides. Nonetheless, the need for additional hardware and software raises system cost and potentially compromises overall robustness. At the circuit level, integrated bidirectional microwave WPT systems employ combined power amplifier and rectifier modules to switch between transmission and reception modes efficiently.

Although this reduces system complexity, these designs are primarily constrained by moderate space transmission efficiency and limited range, limiting their flexibility in diverse environments [7]. Research into bidirectional capacitive power transfer (BCPT) systems highlights challenges in achieving consistent power flow regulation and efficiency, with practical implementation and electromagnetic compatibility issues remaining significant barriers to widespread adoption [8]. Integrated approaches combining wireless power and data transfer via magnetic fields have enhanced power flow control and communication reliability, particularly for electric vehicle applications. Nevertheless, maintaining magnetic alignment and mitigating noise interference in the power and data channels continue to pose operational risks [9]. Finally, developments in bidirectional DC/DC converter topologies for V2G integration have advanced active power flow control between electric vehicles and the grid.

Despite these advances, converter design complexity, control robustness under varying conditions, and scalability to higher power levels remain key limitations [10]. Collectively, these limitations underscore ongoing challenges in achieving precise, stable, scalable bidirectional power flow control in wireless systems, and maintaining synchronization between primary and secondary converters, regulating active and reactive power flow, and ensuring seamless transitions between G2V and V2G modes. These issues motivate the exploration of alternative control techniques, among the available approaches, the PQ-based synchronization control has gained attention for its ability to decouple power direction and magnitude regulation [11]. In this work we adopt and reapply the PQ-based control technique to a 7.7 kW SS-compensated BD-IPT charger, this adopted technique enables: (1) local-only measurement of active (P) and reactive (Q) power (eliminating communication links), (2) decoupled control of power magnitude and direction, and (3) robust synchronization using a VCO-based feedback loop, even amid detuning and misalignment.

The performance of the adopted control method is demonstrated via MATLAB/Simulink simulations aligned with SAE J2954 standards, which specifies operating frequencies (81.39–90 kHz) and power levels (3.7–22 kW) for interoperability [12]. The remainder of this paper is organized as follows: Section **II** presents the modeling of the BD-IPT system, including the fundamental harmonic approximation (FHA) and power flow analysis. Section **III** describes the adopted PQ-based synchronization and power regulation control strategy. Section **IV** provides simulation results and performance evaluation under different operating scenarios. Finally, Section V concludes the paper with key findings and perspectives for future research.

II. MODELING OF THE BIDIRECTIONAL WIRELESS CHARGERS

Figure 1 illustrates the structure of a typical BD-WPT system for EVs. The system begins with a Mains AC Source (50/60 Hz) that is first processed by a bidirectional AC/DC converter is employed to generate a stable DC bus voltage. This is followed by a highfrequency DC/AC converter that generates high frequency AC voltage needed for efficient wireless energy transfer. The AC voltage is then conditioned through a primary compensation network to match the resonant frequency of the loosely coupled transformer, which wirelessly transmits energy across an air gap to the secondary side. The secondary compensation network ensures efficient energy reception. These compensation networks can be classified into four basic topologies: Series-Series (SS), Series-Parallel (SP), Parallel-Parallel (PP), and Parallel-Series (PS), as well as several higher-order configurations like LCC and LCL [13].

In this study, the LC resonant topology was selected as a representative case to analyze the BD-WPT system, the high-frequency AC/DC Converter rectifies the received AC into DC for charging the EV battery. When studying unidirectional wireless chargers, The battery is generally modeled as an equivalent resistance; nevertheless, for bidirectional wireless charging systems, it is more appropriately represented as an equivalent voltage source [14]. In G2V mode, the transmitter side converter functions as a DC/AC inverter, while the receiver side converter acts as a controlled AC/DC rectifier. Conversely, in V2G mode, where the EV battery supplies power back to the grid, the operational roles of the converters are interchanged [15].

A detailed circuit schematic shows that the transmitter side consists of a full-bridge inverter formed by switches Q_{p1} to Q_{p4}, controlled by a primary side controller, and tuned by components C_p. The inverter outputs a high-frequency AC voltage derived from the DC bus voltage V_p, which excites the primary coil L_p. The secondary side mirrors this structure with a full-bridge rectifier formed by switches Q_{s1} to Q_{s4}, controlled by a secondary side controller, and tuned by C_s . The secondary coil L_s. after receiving the wireless power, generates an AC voltage that is rectified to produce the secondary DC bus voltage V_s, which is used for battery charging or to return power to the grid, according to the operation mode. R_p and R_s represent the ESRs of the two sides respectively. The energy transfer is based on mutual inductance M between the transmitter and receiver coils. Compensation networks on both the primary and secondary sides are typically tuned to resonate with the switching frequency. For the SS compensation topology, this implies that [16]:

$$\omega_o = 2\pi f_o = \frac{1}{\sqrt{L_p C_p}} = \frac{1}{\sqrt{L_s C_s}} \tag{1}$$

Where f_o is the switching frequency and ω_o is the angular switching frequency.

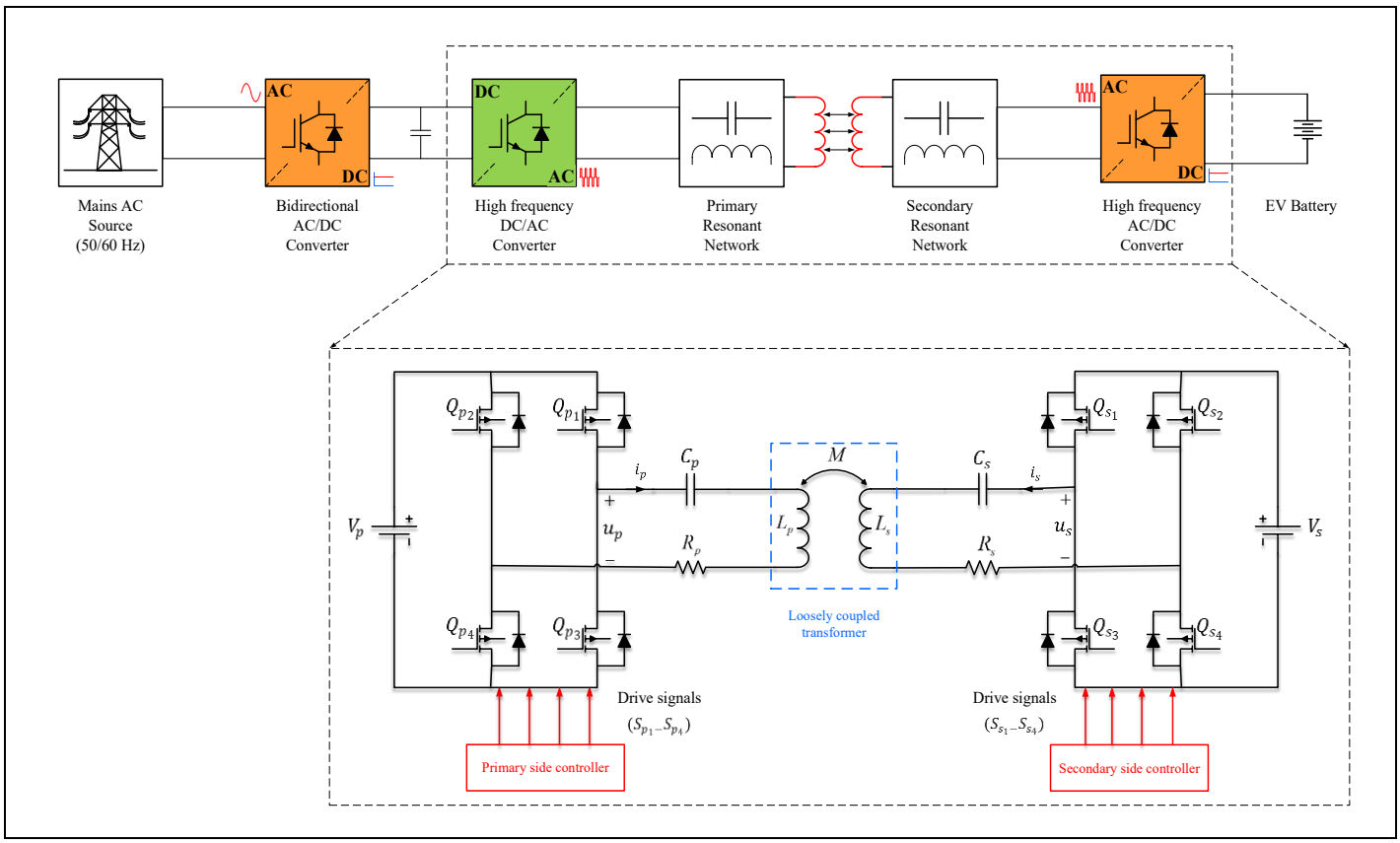

Figure 1: Schematic diagram of the BD-IPT system.
Source: Authors, (2026).

The amount and direction of power exchanged between the two ends of the BD-WPT system can be regulated by managing the magnitudes of the voltages u_p and u_s and the phase angle between them. These voltages are produced using full-bridge converters, both functioning at the switching frequency f_o while maintaining a 50% duty cycle .By introducing phase shifts φ_p on the primary side and φ_s on the secondary side between the two legs of each full-bridge, the converters generate output voltages whose magnitudes can be modulated.

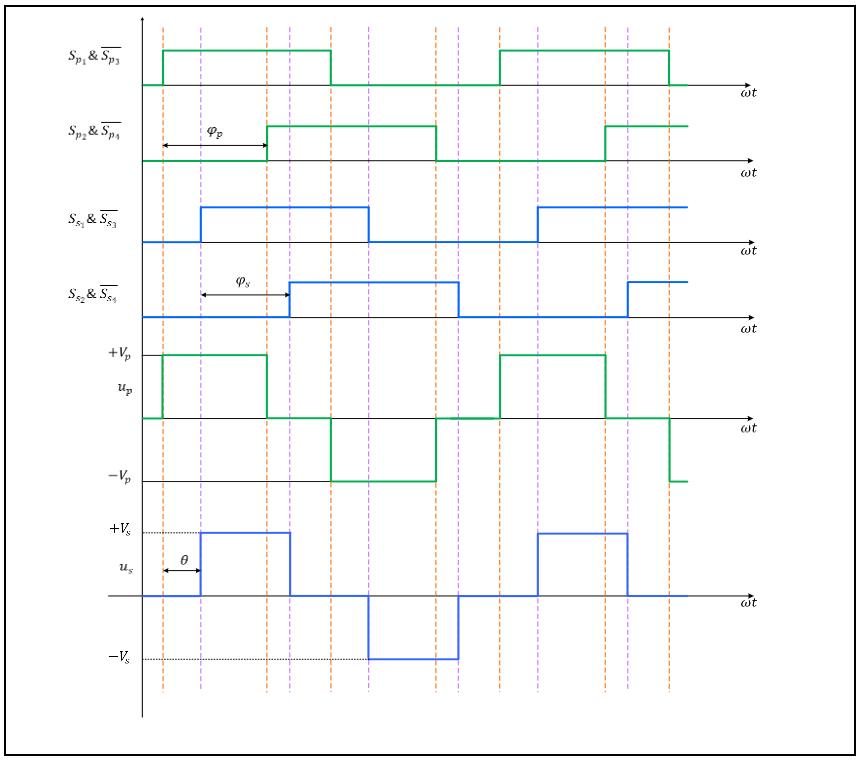

Figure 2: Voltage waveforms of primary and pickup converters.
Source: Authors, (2026).

The direction of power transfer is governed by the relative phase angle θ between primary and secondary voltages: a $+90°$ shift enables charging (grid to EV), while $-90°$ enables discharging (EV to grid), assuming resonant conditions. Figure 2 illustrates typical switching sequences employed to implement this control strategy [11]. Considering one period of the voltage u_p(Figure 3) and applying a phase shift of θ to obtain u_s, both signals can be represented through their Fourier series representation as follows:

$$u_p(t) = \frac{4}{\pi} V_p \sum_{n=1,3,5,\ldots}^{\infty} \frac{1}{n} cos\left(n\omega t + \frac{n\varphi_p}{2}\right) sin\left(\frac{n\varphi_p}{2}\right) \tag{2}$$

$$u_s(t) = \frac{4}{\pi} V_s \sum_{n=1,3,5,\ldots}^{\infty} \frac{1}{n} cos\left(n\omega t + n\theta + \frac{n\varphi_s}{2}\right) sin\left(\frac{n\varphi_s}{2}\right) \tag{3}$$

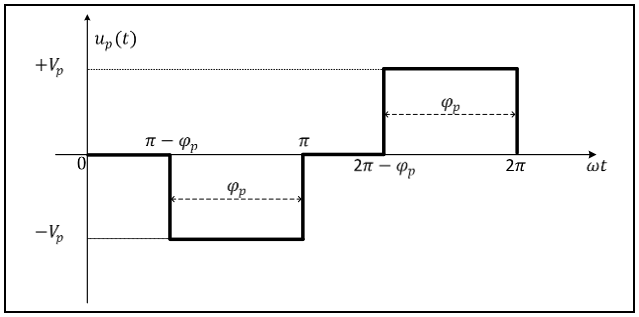

Figure 3: Primary converter output voltage (u_p) waveform over a single switching period.
Source: Authors, (2026).

Since the resonant network exhibits band-pass characteristics, the higher order harmonics can be disregarded, allowing the analysis to focus solely on the fundamental components [17], and the schematic diagram in Figure 1 may be reduced to an equivalent model comprising two voltage sources, and an impedance network, as shown in Figure 4:

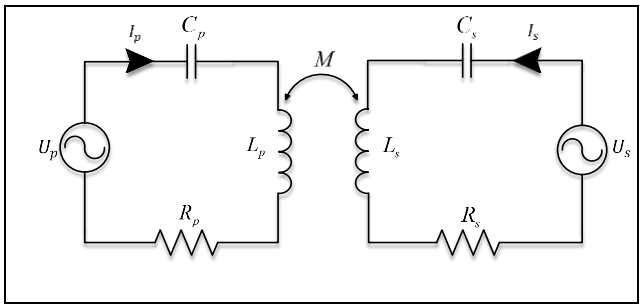

Figure 4: The equivalent circuit of the BD-IPT system.
Source: Authors, (2026).

By adopting the FHA, the steady-state model of the SS-compensated system is obtained as:

$$\begin{cases} \tilde{U}_p = R_p \tilde{I}_p + j\omega M \tilde{I}_s \\ \tilde{U}_s = j\omega M \tilde{I}_p + R_s \tilde{I}_s \end{cases} \tag{4}$$

Where $\tilde{U}_p$ and $\tilde{U}_s$ denote the phasors of the fundamental output voltages of the H-bridge converters on the primary and secondary sides, respectively, The phasor $\tilde{U}_p$ is taken as the reference ($\tilde{U}_p = U_p \angle 0°$) , while the phase angle of $\tilde{U}_s$ is θ, that is, $\tilde{U}_s = U_s \angle \theta$. Moreover, $\tilde{I}_p$ and $\tilde{I}_s$ represent the current phasor on the primary and secondary sides, separately:

$$\tilde{U}_p = \frac{2}{\pi\sqrt{2}} V_p \sin\left(\frac{\alpha}{2}\right) \angle 0° \tag{5}$$

$$\tilde{U}_s = \frac{2}{\pi\sqrt{2}} V_s \sin\left(\frac{\beta}{2}\right) \angle \theta° \tag{6}$$

Solving Equation (4), the primary and secondary currents are:

$$\tilde{I}_p = \frac{R_s \tilde{U}_p - j\omega M \tilde{U}_s}{R_p R_s + (\omega M)^2} \tag{7}$$

$$\tilde{I}_s = \frac{R_p \tilde{U}_s - j\omega M \tilde{U}_p}{R_p R_s + (\omega M)^2} \tag{8}$$

The apparent power of the primary side converter is:

$$S_p = \tilde{U}_p \tilde{I}_p^* = P_p + jQ_p \tag{9}$$

Where P_p and Q_p are the active and reactive power generated by the primary converter and they are given by:

$$P_p = \mathrm{Re}(S_p) = \frac{R_s U_p^2 + \omega M U_p U_s sin(\theta)}{R_p R_s + (\omega M)^2} \tag{10}$$

$$Q_p = \mathrm{Im}(S_p) = \frac{\omega M U_p U_s \cos(\theta)}{\omega R_p R_s + (\omega M)^2} \tag{11}$$

The apparent power absorbed by the secondary side converter is expressed as:

$$S_s = \tilde{U}_s \tilde{I}_s^* = P_s + jQ_s \tag{12}$$

Where P_s and Q_s denote the active and reactive power produced by the secondary side converter and they are given by:

$$P_s = \mathrm{Re}(S_s) = \frac{R_p U_s^2 - \omega M U_p U_s sin(\theta)}{R_p R_s + (\omega M)^2} \tag{13}$$

$$Q_s = \mathrm{Im}(S_s) = -\frac{\omega M U_p U_s \cos(\theta)}{\omega R_p R_s + (\omega M)^2} \tag{14}$$

As such, substitution of Equation (5) and Equation (6) to Equations (9)-(14) and by neglecting resistive terms results in:

$$P_p = \frac{8}{\omega M \pi^2} V_p V_s \sin\left(\frac{\varphi_p}{2}\right) \sin\left(\frac{\varphi_s}{2}\right) \sin(\theta) \tag{15}$$

$$Q_p = \frac{8}{\omega M \pi^2} V_p V_s \sin\left(\frac{\varphi_p}{2}\right) \sin\left(\frac{\varphi_s}{2}\right) \cos(\theta) \tag{16}$$

$$P_s = -\frac{8}{\omega M \pi^2} V_p V_s \sin\left(\frac{\varphi_p}{2}\right) \sin\left(\frac{\varphi_s}{2}\right) \sin(\theta) \tag{17}$$

$$Q_s = -\frac{8}{\omega M \pi^2} V_p V_s \sin\left(\frac{\varphi_p}{2}\right) \sin\left(\frac{\varphi_s}{2}\right) \cos(\theta) \tag{18}$$

To describe the power flow at the pickup side, the power phase angle is expressed as:

$$\theta_{Power} = \arccos\left(\frac{P_s}{\sqrt{P_s^2 + Q_s^2}}\right) \tag{19}$$

$$\theta_{Power} = \arccos[-\sin(\theta)] \tag{20}$$

From Equation (15) and Equation (17), it follows that when $\theta \in [-\pi, 0]$, with $P_p < 0$ and $P_s > 0$, the primary-side voltage lags the secondary-side voltage, thus enabling power flow from the secondary side back to the primary side.

Conversely, in cases where $\theta \in [0, \pi]$, with $P_s < 0$ and $P_p > 0$, the primary-side voltage leads the secondary-side voltage, and power flows from the primary to the secondary side. When $\theta = -/+ 90°$ (which is consistent with a power angle θ_{Power} of 0° or 180°, respectively), from Equation (16) and Equation (18), the output reactive power of the primary and secondary converters becomes zero, while the active power attains its maximum value.

III. THE SYNCHRONIZATION TECHNIQUE CONTROL

In the BD-WPT system, a PQ-based controller is adopted for the secondary side to regulate power transfer by processing the measured voltage and current to compute the power flow and the relative phase angle between the primary and secondary voltages $\widetilde{U}_p$ and $\widetilde{U}_s$ (Figure 5). The control scheme consists of two coordinated loops: one for synchronizing the converters and controlling the direction of power flow, and another for regulating the transferred active power. A VCO aligns the pickup switching frequency by minimizing the difference between the calculated power phase angle and its reference $\theta_{\text{P\_ref}}$, with the error corrected through a PI controller to adjust the relative phase angle θ. In parallel, the measured active power is compared with its reference P_{ref}, and the error is processed by an independent PI regulator to generate a variable φ_s for amplitude modulation, enabling decoupled control of power direction and magnitude [11].

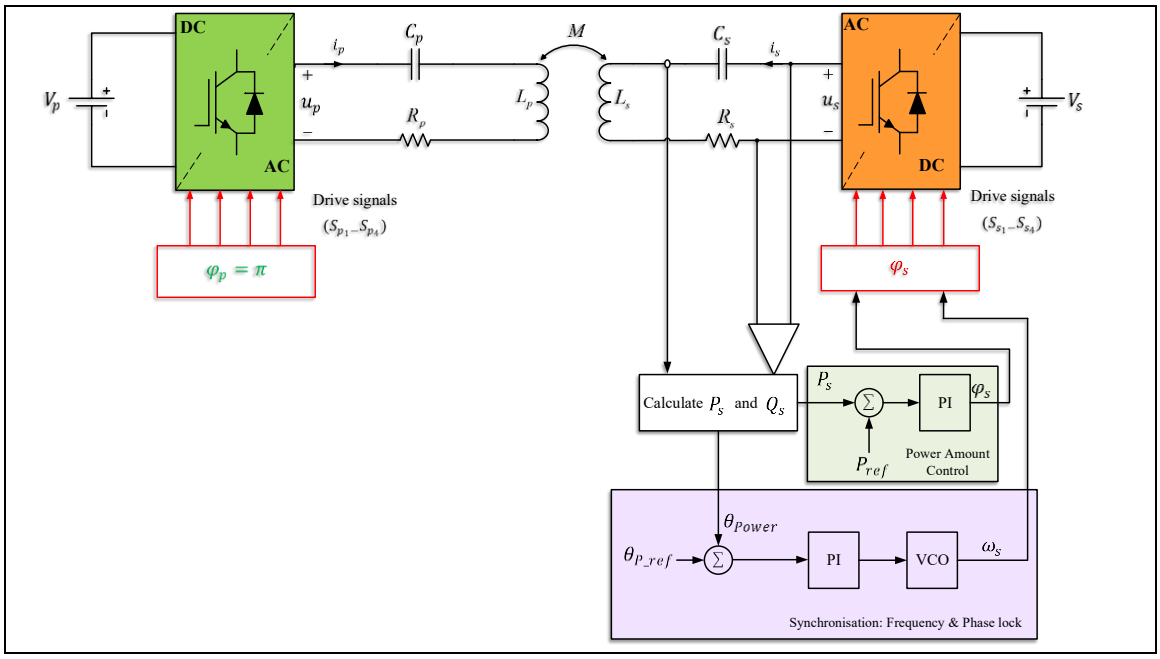

Figure 5: Synchronization and transferring power amount control technique.
Source: Authors, (2026).

Since the synchronization loop relies on the accuracy of the calculated power phase angle, a correction algorithm (Figure 6) is introduced to eliminate ambiguity caused by the non-monotonic behavior θ_{Power}, ensuring a continuous and robust mapping between the estimated and actual relative phase angle.

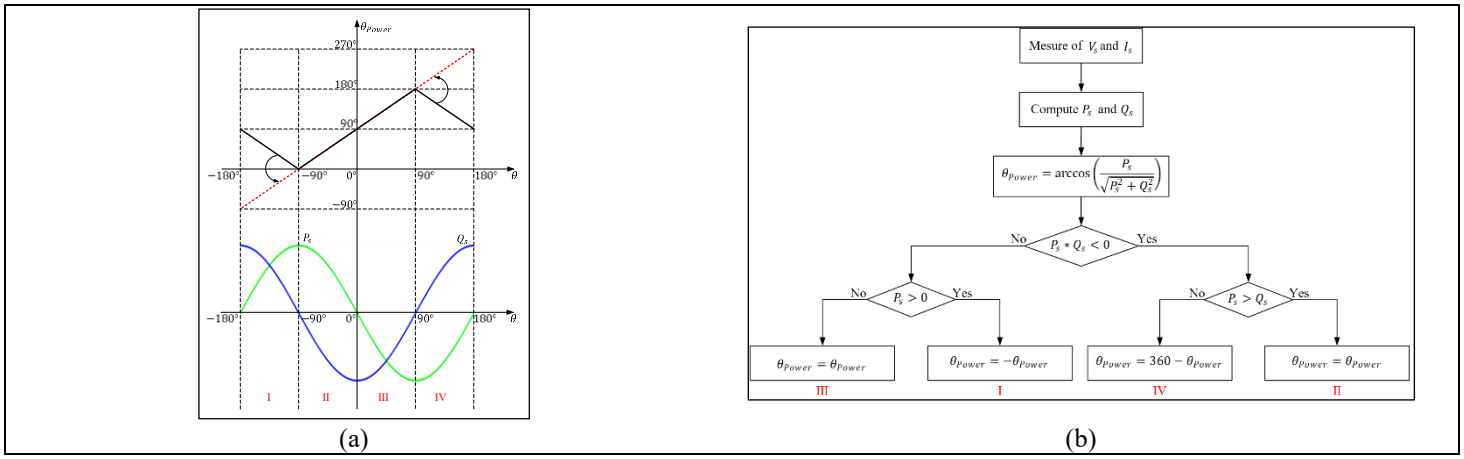

(a) (b)

Figure 6: (a) Power and phase angle characteristics. (b) Correction algorithm.
Source: Authors, (2026).

In Figure 6(a), the solid curves illustrate the active and reactive powers obtained from Equations (17)–(18), together with the power phase angle from Equation (19), plotted as functions of the relative phase angle θ under resonant operation. It can be observed that θ_{Power} increases monotonically in Regions II and III, but shows a decreasing trend in Regions I and IV as θ varies from $-180°$ to $180°$.

To eliminate this discontinuity, the correction procedure shown in Figure 6(b) is applied, which modifies the values of θ_{Power} in Regions III and IV to establish a continuous mapping between θ_{Power} and θ.

IV. SIMULATION RESULTS AND DISCUSSIONS

In order to validate the effectiveness of the adopted PQ-based control strategy for BD-WPT, different test scenarios were conducted to demonstrate both synchronization performance and power regulation capability using MATLAB software, considering the defined system parameters listed in Table 1. These parameters comply with the SAE J2954 standards. As specified in the SAE technical information report J2954, WPT systems should operate within the frequency range of 81.39–90 kHz. Furthermore, SAE J2954 categorizes wireless power transfer systems into four power levels: 3.7 kW, 7.7 kW, 11 kW, and 22 kW [12], [18]. The simulation setup adheres to the SAE J2954 WPT standards while remaining consistent with the lithium-ion battery voltage range (300–600 V) typically used in EVs.

Table 1: System parameters.

Parameter	Symbol	Nominal Value
Power output level	P_o	$7.7\ kW$
Input DC voltage	V_{in}	$240\ V$
Switching frequency	f_s	$85\ kHz$
Primary side compensation capacitance	C_p	$93.045\ nF$
Primary side self-inductance	L_p	$37.68\ \mu H$
Primary side ESR	R_p	$0.01\ \Omega$
Secondary side compensation capacitance	C_s	$64.87\ nF$
Secondary side self-inductance	L_s	$54.04\ \mu H$
Secondary side ESR	R_s	$0.01\ \Omega$
Mutual inductance of the coupled coils	M	$9.025\ \mu H$
Output Filter capacitor	C_o	$220\ \mu F$
Load resistance	R_o	$20.78\ \Omega$

Source: Authors, (2026).

Figure 7(a) illustrates the time-domain waveforms during maximum power transfer from the transmitter to the receiver side. The synchronization system operates by detecting the active and reactive powers, followed by adjusting the delay and duty cycle of the pickup control signals. By means of a VCO controller, the power phase is tracked to maintain a fixed 90° phase difference between the primary and secondary voltages. Consequently, the transferred power initially oscillates but eventually stabilizes at the reference value, while the pickup voltage locks in phase with the primary voltage and both active and reactive powers reach steady-state conditions.

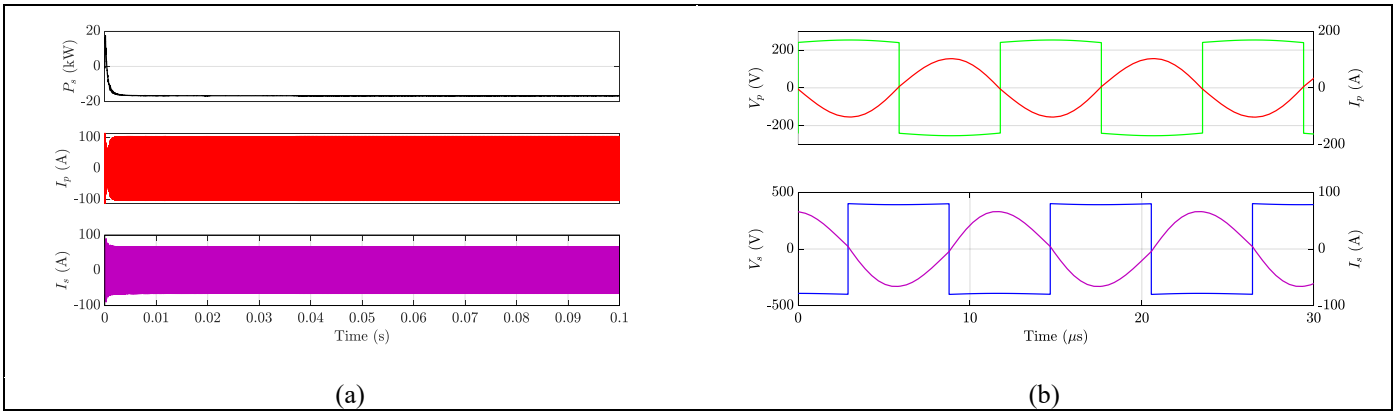

Figure 7: Waveforms under forward maximum power transfer: (a) active power and current profiles.
Source: Authors, (2026).

From Figure 7(b) the primary inverter voltage u_p (fixed square wave) leads the secondary inverter voltage u_s (which also exhibits a square shape under maximum power transfer conditions, where the secondary phase modulation φ_s reaches its maximum value of 180°) by 90°, this corresponds to maximum forward power transfer under resonant conditions, validating the PQ-based controller in achieving synchronization and stable operation in G2V mode. Figure 8(a) shows the transient response of active power and current profiles during the reversal of power transfer from forward (G2V) to reverse (V2G).

Furthermore, Figure 8(b)-(c) illustrates the voltage and current waveforms when 7.7 kW is delivered to the secondary side and when it is delivered back to the primary side. The transition is achieved by adjusting the relative phase angle between the primary and secondary voltages from $+90°$ to $-90°$. During this process, the controller successfully regulates synchronization, and the current profiles

adapt without significant distortion. In forward power flow (Figure 8(b)), V_p leads V_s by 90°, while in reverse power flow (Figure 8(c)), V_s leads V_p by 90°, confirming bidirectional capability.

Importantly, the magnitude of the voltages and currents remains similar in both directions, showing that the controller maintains symmetrical performance for G2V and V2G operation. This result demonstrates the PQ-based controller's effectiveness in enabling smooth bidirectional transitions without destabilizing the system.

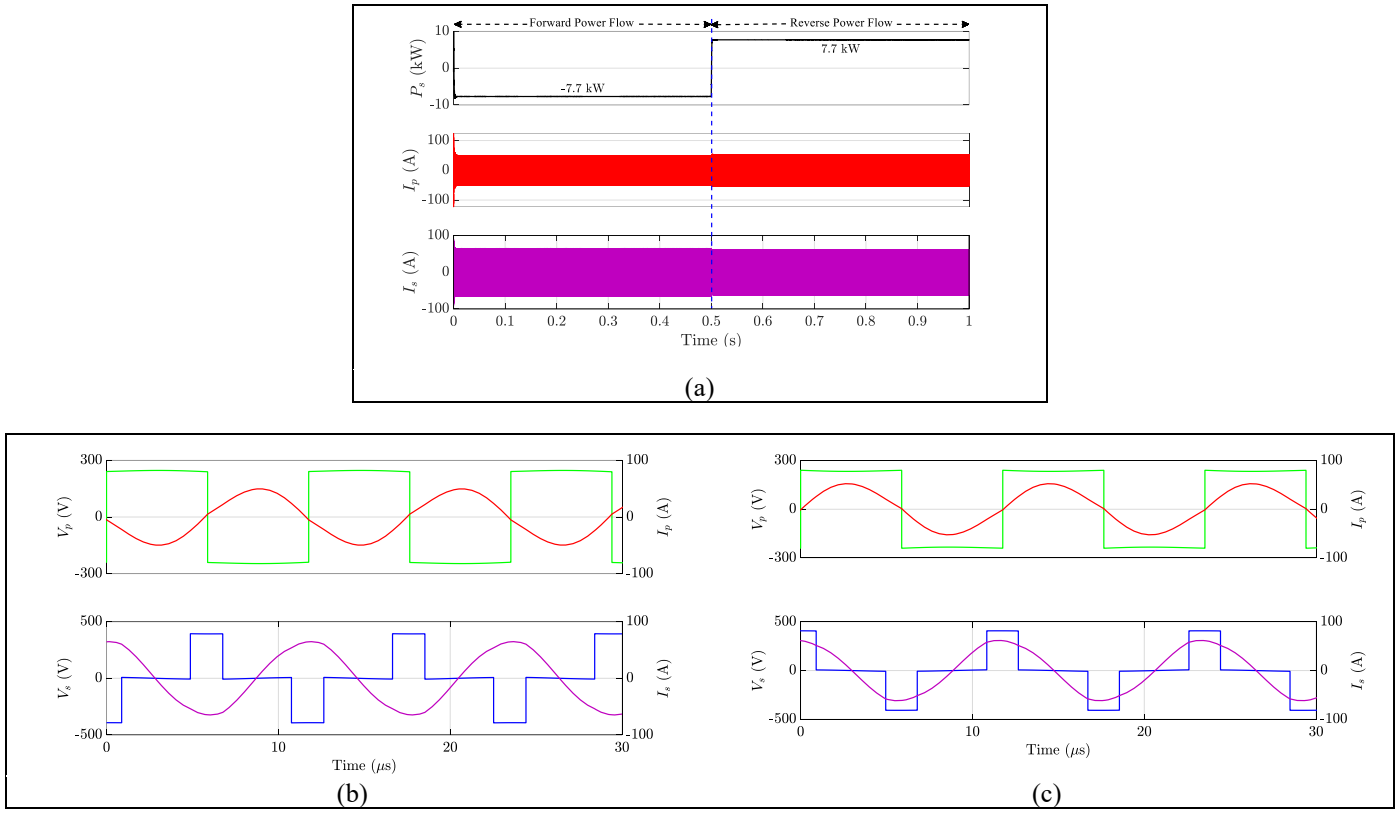

Figure 8: Waveforms during reversal of power transfer direction: (a) active power and current profiles, enlarged view of voltage and current waveforms: (b) under forward flow (c) under reverse flow.
Source: Authors, (2026).

Figure 9(a) shows the active power and current profiles when the reference power is reduced from –7.7 kW to –3.3 kW at 0.5 s. Figure 9(b) and 9(c) illustrate the corresponding voltage and current waveforms for each operating point. The controller adjusts the duty cycle of the secondary voltage V_s to match the new power reference. The results confirm that the PQ-based strategy can decouple power regulation from synchronization, since synchronization remains locked while the amplitude of transferred power is varied. The transient is smooth, and the system quickly stabilizes at the new reference power level, demonstrating the controller's robustness. These results indicate that the PQ-based approach enables accurate power regulation while maintaining phase synchronization.

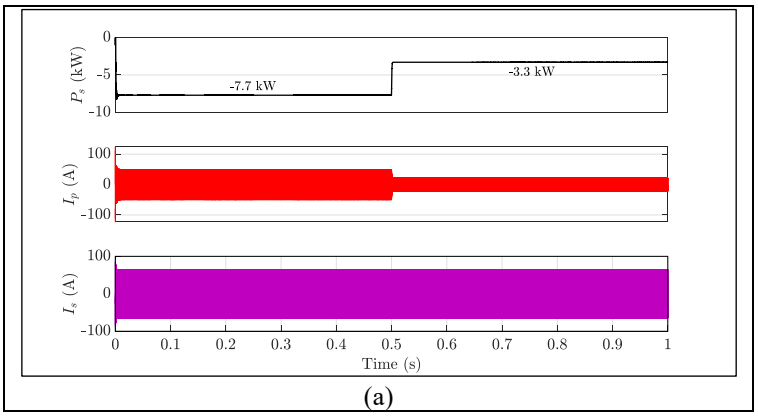

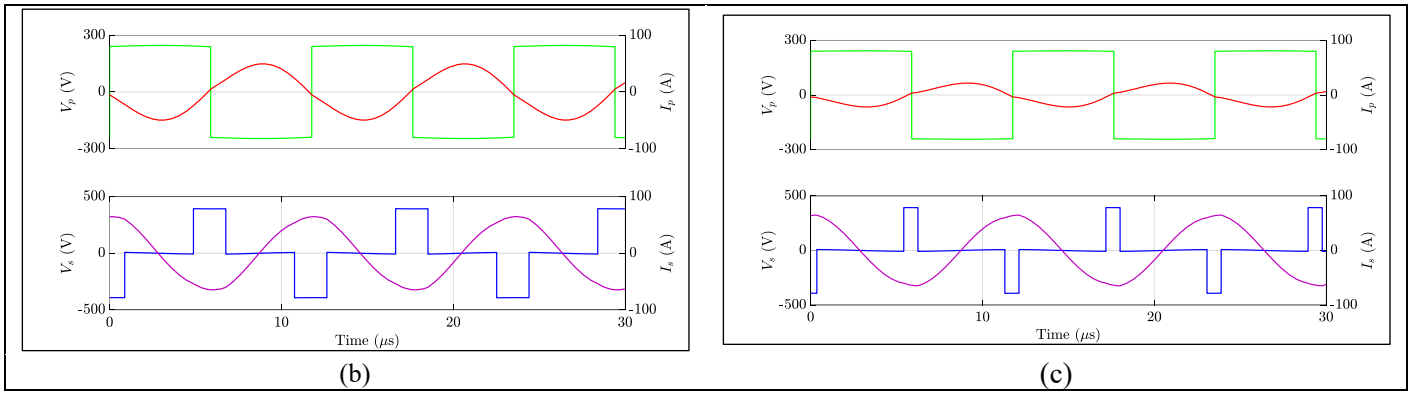

Figure 9: Waveforms during the power transition from $-7.7\ kW$ to $-3.3\ kW$: (a) active power and current profiles, enlarged view of voltage and current waveforms: (b) when transmitting $-7.7\ kW$ (c) when transmitting $-3.3\ kW$.
Source: Authors, (2026).

When the secondary resonant capacitor C_s is increased from its designed value of $64.87\ nF$ to $74.67\ nF$, the system operates under a detuned condition that alters the resonance balance between the primary and secondary circuits, and the resonance condition is no longer satisfied at the operating frequency of $85\ kHz$.

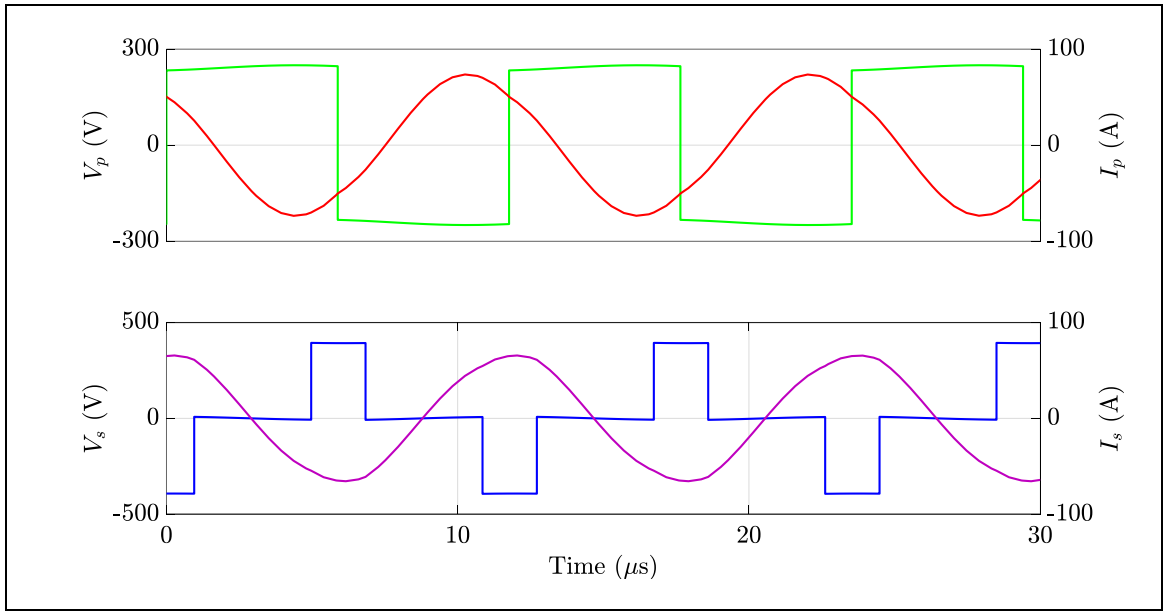

Figure 10: Voltage and current characteristics under detuned resonance.
Source: Authors, (2026).

As shown in Figure 10, this detuning mainly manifests on the primary side: the primary current I_p exhibits a clear phase displacement relative to the primary voltage V_p. In contrast, the secondary current I_s remains aligned with the secondary voltage V_s (but with negative polarity), indicating that the local resonance on the secondary side is preserved with respect to its driving voltage. This phenomenon occurs because variations in C_s modify the reflected impedance seen by the primary, thereby shifting the phase relationship between V_p and I_p and influencing the overall power flow.

Such detuning conditions emphasize the importance of the PQ-based synchronization control strategy, which decouples active and reactive power regulation. By accurately synchronizing the converter operation and controlling the power components, the PQ method enables the system to deliver the desired active power while keeping the reactive power at a minimum, even when parameter mismatches or resonance deviations occur.

To evaluate the robustness of the proposed PQ-based synchronization control, Figure 11 presents the primary and secondary voltage and current waveforms under a misalignment condition. The lateral displacement between the transmitting and receiving coils is modeled as a reduction in the coupling coefficient from 0.2 to 0.1, while maintaining a transferred power of 7.7 kW to the secondary side. Despite the weakened magnetic coupling, the controller successfully regulates active and reactive power by reducing the magnitude of the secondary voltage V_s. This confirms the capability of the PQ-based control strategy to sustain reliable power transfer and minimize reactive components even under significant coupling variations.

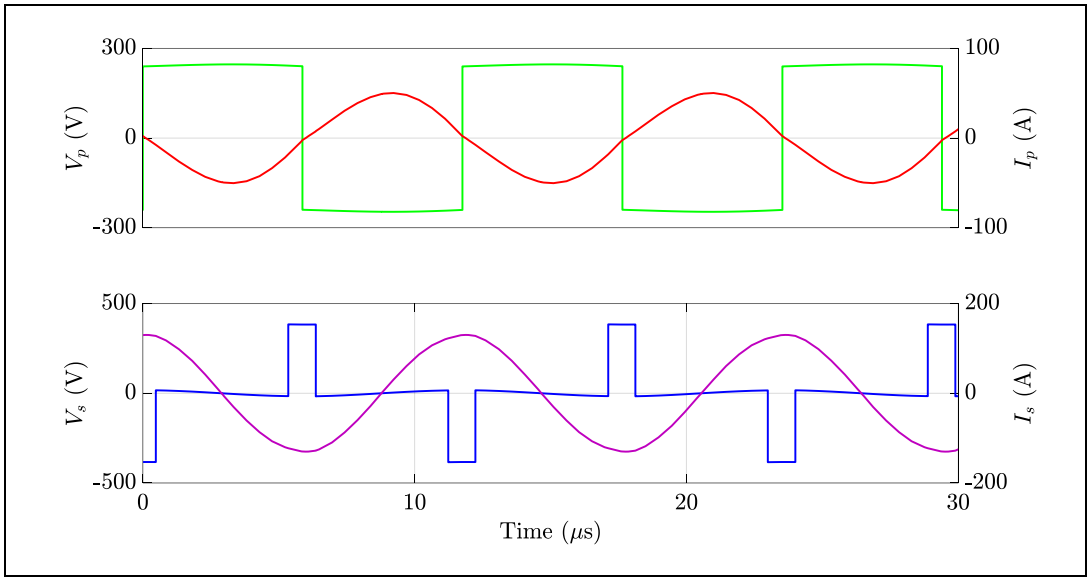

Figure 11: Voltage and current waveforms under coil misalignment.
Source: Authors, (2026).

V. CONCLUSIONS

This work presented a PQ-based synchronization and control strategy for BD-WPT systems, applied to a 7.7 kW SS-compensated charger. By utilizing only local measurements of active and reactive power, the method eliminates communication requirements, thereby reducing system cost and complexity. The adoption of a VCO-based feedback loop ensures robust synchronization while enabling independent regulation of power direction and magnitude. Simulation results verified the controller's effectiveness under various scenarios, including forward and reverse power transfer, dynamic reference tracking, resonance detuning, and coil misalignment. The results confirm that the proposed PQ-based approach provides accurate, stable, and symmetric performance in both G2V and V2G modes. Future work will focus on experimental validation and extending the method to higher power levels and multi-vehicle charging scenarios, further advancing the deployment of BD-WPT systems in smart grid applications.

VI. AUTHOR'S CONTRIBUTION

Conceptualization: Abdelmoumin Hamrani, Abdelhalim Tlemçani and Said Barkat.
Methodology: Abdelmoumin Hamrani, Abdelhalim Tlemçani and Said Barkat.
Investigation: Abdelmoumin Hamrani, Abdelhalim Tlemçani and Said Barkat.
Discussion of results: Abdelmoumin Hamrani, Abdelhalim Tlemçani and Said Barkat.
Writing – Original Draft: Abdelmoumin Hamrani, Abdelhalim Tlemçani and Said Barkat.
Writing – Review and Editing: Abdelmoumin Hamrani, Abdelhalim Tlemçani and Said Barkat.
Resources: Abdelmoumin Hamrani, Abdelhalim Tlemçani and Said Barkat.
Supervision: Abdelmoumin Hamrani, Abdelhalim Tlemçani and Said Barkat.
Approval of the final text: Abdelmoumin Hamrani, Abdelhalim Tlemçani and Said Barkat.

VIII. REFERENCES

[1] R. P. Upputuri and B. Subudhi, "A Comprehensive Review and Performance Evaluation of Bidirectional Charger Topologies for V2G/G2V Operations in EV Applications," IEEE Trans. Transp. Electrification, vol. 10, no. 1, pp. 583–595, Mar. 2024, doi: 10.1109/TTE.2023.3289965.

[2] Md. R. H. Mojumder, F. Ahmed Antara, Md. Hasanuzzaman, B. Alamri, and M. Alsharef, "Electric Vehicle-to-Grid (V2G) Technologies: Impact on the Power Grid and Battery," Sustainability, vol. 14, no. 21, p. 13856, Oct. 2022, doi: 10.3390/su142113856.

[3] A. Munsi, S. Pradhan, and K. Aditya, "Perspectives on control strategies for CC-CV charging in Resonant Inductive Power Transfer systems: a review of SS-RIPT configuration," Wirel. Power Transf., vol. 11, no. 1, pp. 0–0, 2024, doi: 10.48130/wpt-0024-0009.

[4] M. Sun, X. Dai, L. Wang, D. Kang, and X. Lv, "Inherent resonance frequency dynamic tacking method with misalignment of coupling plates for the bidirectional EC-WPT system," Wirel. Power Transf., vol. 12, no. 1, pp. 0–0, 2025, doi: 10.48130/wpt-0025-0002.

[5] F. Liu, K. Li, K. Chen, and Z. Zhao, "A Phase Synchronization Technique Based on Perturbation and Observation for Bidirectional Wireless Power Transfer System," IEEE J. Emerg. Sel. Top. Power Electron., vol. 8, no. 2, pp. 1287–1297, June 2020, doi: 10.1109/JESTPE.2019.2942101.

[6] W. Ye, T. Götz, B. Qi, and N. Parspour, "A Communication-Based Synchronization and Control Method for Bidirectional Wireless Power Transfer System," in IECON 2023- 49th Annual Conference of the IEEE Industrial Electronics Society, Oct. 2023, pp. 1–6. doi: 10.1109/IECON51785.2023.10311922.

[7] X. Zhang, Y. Liu, P. Zhang, Z. Chen, and Y. Wei, "An integrated power conversion system for bidirectional microwave wireless power transfer," Wirel. Power Transf., vol. 12, no. 1, pp. 0–0, 2025, doi: 10.48130/wpt-0025-0003.

[8] Y. Wu, U. K. Madawala, L. Zhao, and X. Dai, "Research Status of Bidirectional Wireless Power Transfer Technology," Green Energy Intell. Transp., p. 100266, Feb. 2025, doi: 10.1016/j.geits.2025.100266.

[9] J. Kao, C. Lin, C. Huang, and Y. Kuo, “Bidirectional wireless power/data transfer via magnetic field,” J. Eng., vol. 2022, no. 7, pp. 701–714, July 2022, doi: 10.1049/tje2.12150.

[10] M. Venkatesan, N. R, P. Kacor, and M. Vrzala, “Bidirectional wireless power transfer: Bridging electric vehicles and the grid through converter analysis, coil topologies, and communication protocol review,” Results Eng., vol. 25, p. 103803, Mar. 2025, doi: 10.1016/j.rineng.2024.103803.

[11] Y. Tang, Y. Chen, U. K. Madawala, D. J. Thrimawithana, and H. Ma, “A New Controller for Bidirectional Wireless Power Transfer Systems,” IEEE Trans. Power Electron., vol. 33, no. 10, pp. 9076–9087, Oct. 2018, doi: 10.1109/TPEL.2017.2785365.

[12] H. Das, M. Rahman, S. Li, and C. W. Tan, “Electric vehicles standards, charging infrastructure, and impact on grid integration: A technological review,” Renew. Sustain. Energy Rev., vol. 120, p. 109618, Nov. 2019, doi: 10.1016/j.rser.2019.109618.

[13] S. Meraj, S. Mekhilef, M. Binti Mubin, H. Ramiah, M. Seyedmahmoudian, and A. Stojcevski, “Bidirectional Wireless Charging System for Electric Vehicles: A Review of Power Converters and Control Techniques in V2G Application,” IEEE Access, vol. 13, pp. 75246–75264, 2025, doi: 10.1109/ACCESS.2025.3561396.

[14] A. Triviño, J. M. Gonzalez-Gonzalez, and M. Castilla, “Review on Control Techniques for EV Bidirectional Wireless Chargers,” Electronics, vol. 10, no. 16, p. 1905, Aug. 2021, doi: 10.3390/electronics10161905.

[15] M. Venkatesan, R. Narayanamoorthi, K. M. AboRas, and A. Emara, “Efficient Bidirectional Wireless Power Transfer System Control Using Dual Phase Shift PWM Technique for Electric Vehicle Applications,” IEEE Access, vol. 12, pp. 27739–27755, 2024, doi: 10.1109/ACCESS.2024.3367437.

[16] S. Jia, C. Chen, P. Liu, and S. Duan, “A Digital Phase Synchronization Method for Bidirectional Inductive Power Transfer,” IEEE Trans. Ind. Electron., vol. 67, no. 8, pp. 6450–6460, Aug. 2020, doi: 10.1109/TIE.2019.2939979.

[17] S. Jia, C. Chen, S. Duan, and Z. Chao, “Dual-Side Asymmetrical Voltage-Cancelation Control for Bidirectional Inductive Power Transfer Systems,” IEEE Trans. Ind. Electron., vol. 68, no. 9, pp. 8061–8071, Sept. 2021, doi: 10.1109/TIE.2020.3016265.

[18] A. Sagar et al., “A Comprehensive Review of the Recent Development of Wireless Power Transfer Technologies for Electric Vehicle Charging Systems,” IEEE Access, vol. 11, pp. 83703–83751, 2023, doi: 10.1109/ACCESS.2023.3300475.